Environmental Satellite Processing Center

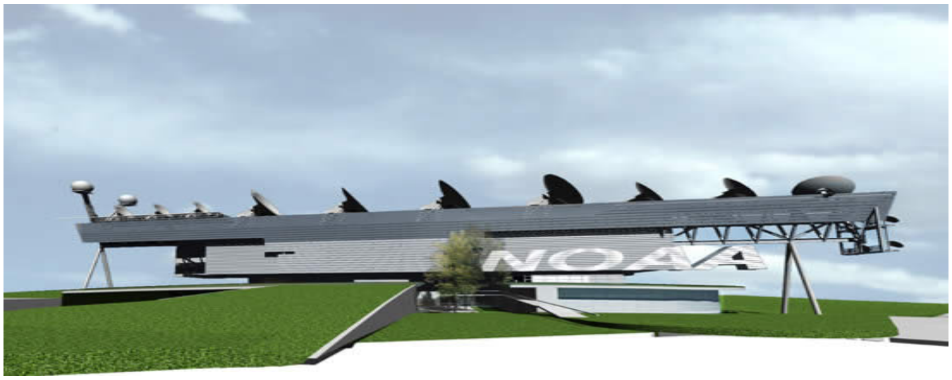

VIIRS Surface Reflectance

Algorithm Theoretical Basis Document

Version 3.0

TITLE: VIIRS SURFACE REFLECTANCE ALGORITHM THEORETICAL BASIS DOCUMENT

AUTHORS:

E. Vermote (NASA), B. Franch (University of Maryland), J.C. Roger (University of Maryland)

Ivan Csiszar (NOAA/NESDIS Center for Satellite Applications and Research)

Remarks:

This document shares algorithm descriptive material with the following documents:

1. Joint Polar Satellite System (JPSS) VIIRS Surface Reflectance Algorithm Theoretical Basis Document (ATBD) Revision A. Joint Polar Satellite System (JPSS) Ground Project Code 474; 474-00034; September 18, 2013
2. corresponding NASA-sponsored VIIRS Surface Reflectance algorithm theoretical basis document (Suomi-NPP VIIRS Surface Reflectance Algorithm Theoretical Basis Document (ATBD); Version 2.0, October 10th, 2016

DOCUMENT HISTORY
DOCUMENT REVISION LOG

The Document Revision Log identifies the series of revisions to this document since the baseline release. Please refer to the above page for version number information.

DOCUMENT TITLE: Algorithm Theoretical Basis Document Template			
DOCUMENT CHANGE HISTORY			
Revision No.	**Date**	**Revision Originator Project Group**	**CCR Approval # and Date**
2.1	1/23/2018	Origonal NDE version of the ATBD	
2.2	3/5/2018	Minor editorial changes (I. Csiszar)	
3.0	11/27/2018	Update to Operation (H. Ding, Y. Zhu)	CCR7618

LIST OF CHANGES

Significant alterations made to this document are annotated in the List of Changes table.

DOCUMENT TITLE: Algorithm Theoretical Basis Document Template

LIST OF CHANGE-AFFECTED PAGES/SECTIONS/APPENDICES

Version Number	Date	Changed By	Page	Section	Description of Change(s)
2.2	3/5/2018	Csiszar, I.	2		Added NASA ATBD title and version

TABLE OF CONTENTS

Page

LIST OF TABLES AND FIGURES

1. INTRODUCTION

This document presents the scientific background, design and anticipated performance of the Surface Reflectance (SR) algorithm for the Joint Polar Satellite System (JPSS). The SR algorithm produces directional surface reflectance values for Visible Infrared Imaging Radiometer Suite (VIIRS) band centered at 0.412 μm, 0.445 μm, 0.488 μm, 0.555 μm, 0.645 μm, 0.672 μm, 0.865 μm (two different spatial resolutions), 1.24 μm, 1.61 μm (two different spatial resolutions), and 2.25 μm. It is an algorithm for surface reflectance retrieval that has been derived from Moderate Resolution Imaging Spectroradiometer (MODIS).

The VIIRS SR algorithm described here fulfills the requirements defined in the JPSS ESPC Requirements Document (JERD). Furthermore, those requirements provide continuity to the Moderate Resolution Imaging Spectroradiometer (MODIS) and the Advanced Very High Resolution Radiometer (AVHRR) surface reflectance data records. The VIIRS surface reflectance algorithm is based on a long heritage most recently coming from MODIS (Vermote et al., 1994; 1997; 2014; Vermote and Vermeulen, 1999). The spectral and spatial characteristics of the MODIS sensor are generally similar to the spectral and spatial requirements of the VIIRS sensor.

1.1. Product Overview

1.1.1. Product Description

The algorithm described in this document produces the Surface Reflectance Environmental Data Record (EDR), one of over thirty products to be generated from the Visible Infrared Imaging Radiometer Suite (VIIRS). The VIIRS prototype is carried onboard the Suomi National Polar-orbiting Partnership Project (NPP) spacecraft. The Surface Reflectance EDR consists of directional surface reflectance values in bands centered at 0.412 µm, 0.445 µm, 0.488 µm, 0.555 µm, 0.645 µm, 0.672 µm, 0.865 µm (two different spatial resolutions), 1.24 µm, 1.61 µm (two different spatial resolutions), and 2.25 µm. It is an algorithm for surface reflectance retrieval that has been derived from Moderate Resolution Imaging Spectroradiometer.

1.2. Satellite Instrument Description

The SR algorithm uses data from the VIIRS instrument on the Suomi National Polar-orbiting Partnership (S-NPP) platform and on subsequent satellites of the Joint Polar Satellite System (JPSS). S-NPP was launched on October 28, 2011, while NOAA-20 was launched as JPSS-1 on November 18, 2017. Both are in a sun synchronous orbits with a 1:30pm ascendingnode orbit half an orbit apart, at mean altitudes of approximately 829 km and 825km, respectively.

The VIIRS instrument is a whiskbroom scanning radiometer with a swath width of 3060 km, providing full daily coverage both in the day and night side of the Earth. It has 22 spectral bands covering the spectrum between 0.412 µm and 12.01 µm, including 16 moderate resolution bands (M-bands) with a spatial resolution of 750 m at nadir, 5 imaging resolution bands (I-bands) – with a spatial resolution of 375 m at nadir, and one panchromatic DNB with a 750 m spatial resolution throughout the scan. Further details can be found in the VIIRS Sensor Data Record (SDR) User's Guide (NOAA Technical Report NESDIS 142A).

At the time of the preparation of this document, NOAA-20 was in its early orbit checkout phase. All subsequent discussions and results refer to the Suomi NPP product only.

2. ALGORITHM DESCRIPTION

2.1. Processing Outline

The Surface Reflectance EDR algorithm is designed to contain four main subroutines: Extract inputs, Quality Flags, Surface Reflectance Retrieval and Write Surface Reflectance EDR. The Surface Reflectance Retrieval subroutine is the main subroutine since it performs the lambertian approximation (atmospheric correction), the adjacency adjustment, and the bidirectional reflectance distribution function (BRDF) coupling adjustment.

The Surface Reflectance Retrieval routine corrects for the effects of gaseous absorption, molecular and aerosol scattering, thin cirrus contamination, glare from surrounding surface pixels (adjacency adjustment), and the coupling of the atmosphere and the surface bidirectional reflectance as a function of the viewing and solar geometries, elevation of the target and spectral band. The atmospheric adjustment (within the 'Surface Reflectance Retrieval' routine) includes updating the correction coefficients with 'in-view' total column water vapor, ozone, and aerosol optical thickness data input fields. The aerosol information required for surface reflectance retrieval comes from the VIIRS Aerosol Optical Thickness (AOT) EDR and the Aerosol Model Information IP, complemented by total column water vapor, total column ozone, and surface pressure from National Centers for Environmental Prediction (NCEP) feeds. Backups for these inputs include total column ozone from the Ozone Mapping Profiling Suite (OMPS). The atmospherically corrected surface reflectance values derived using the Lambertian approximation are subsequently adjusted for adjacency and bi-directional reflectance distribution function (BRDF) effects. The BRDF-coupling adjustment is presently designed after the MODIS approach with a slight modification making the isotropic shape parameter a function of the normalized difference vegetation index, NDVI, (Vermote, 2003), an approximation due to operational constraints and the developmental maturity of the MODIS BRDF-coupling adjustment routine. The surface reflectance values after each adjustment are included as data layers in the surface reflectance EDR along with the Land Quality Flags. The atmospheric inputs are available elsewhere, and the solar and viewing geometries are kept as part of the SDR.

Thin cirrus effects are removed by implementing an empirically based correction using VIIRS band M9 (1.38 μm). The quality control (QC) flags generated from the Build SDR module and the cloud and aerosol quality flag inputs are fused into a single Land Quality Flag (LQF) structure that applies to the Surface Reflectance EDR, the Surface Albedo EDR, the Vegetation Index EDR, the Surface Type EDR. The LQF output is appended to the Surface Reflectance EDR. Then the heart of the surface reflectance retrieval process begins, by converting the cirrus effects adjusted satellite reflectance values into surface reflectance values assuming the surface is Lambertian. The earth's surface is generally not Lambertian, and as a result a further correction is applied. The conversion of the at-satellite-reflectance values to surface reflectance requires (i) the use of a set of conversion equations that also account for first order atmospheric multiple scattering effects, and (ii) inputs from pre-generated look up tables (LUTs) and analytic equations for gaseous or molecular effect.

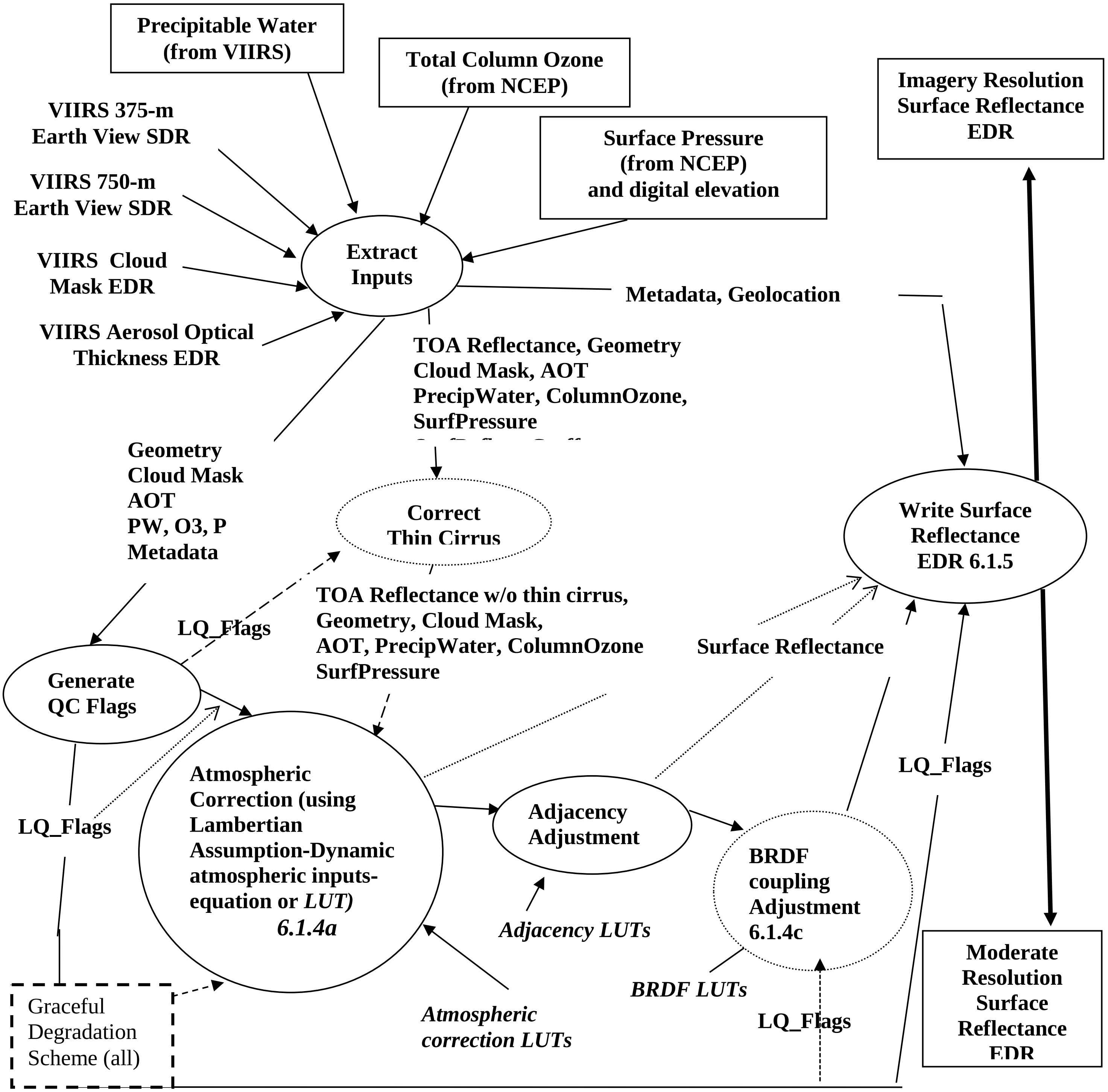

Figure 1. Surface Reflectance EDR processing architecture.

The Lambertian surface reflectance value is passed simultaneously into the adjacency subroutine and to the 'write surface reflectance EDR' routine. The output of the adjacency adjustment subroutine is simultaneously passed to the 'write surface reflectance EDR' routine and to the BRDF-coupling adjustment subroutine. Some land quality (LQ) flags may be required during processing within the BRDF-coupling subroutine. The output of the BRDF–coupling adjustment routine is then passed to the 'write surface reflectance EDR'. The requirements for the VIIRS Surface Reflectance product are described in Volume 2 of the JPSS ESPC Requirements Document.

2.2. Theoretical Description

2.2.1 Introduction

The retrieval of surface reflectance requires calibrating the sensor input to reflectance units, and removing the relatively small contribution due to the atmosphere. The principal atmospheric components affecting the top-of-atmosphere (TOA), or at-satellite-reflectance in the range of 0.4-2.5 µm are shown in Figure 2.

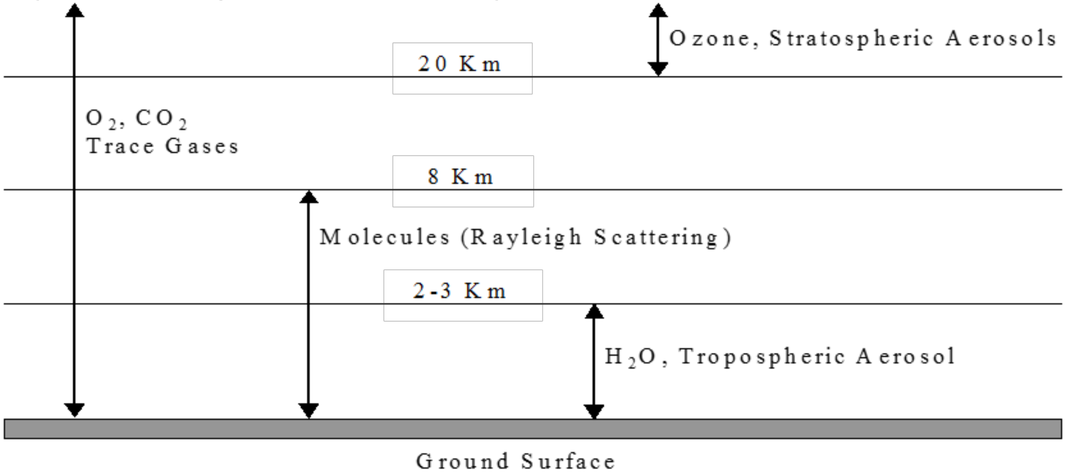

Figure 2. The atmospheric components affecting the remote sensing signal in the 0.4-2.5 µm range.

2.2.2 Lambertian correction

2.2.2.1 Formalism

Using the formalism developed for the 6S code, the solution of the radiation transfer equation employing the Lambertian Uniform Target assumption for observation in electro-optical spectral band i, assuming a standard atmospheric profile, but variable ozone and water vapor amount, is written as (Vermote *et al.*,1997):

$$\rho^i_{TOA}(\theta_s,\theta_v,\varphi,P,Aer^i,U_{H_2O},U_{O_3}) = Tg^i_{OG}(m,P)Tg^i_{O_3}(m,U_{U_{O_3}})[\rho^i_{atm}(\theta_s,\theta_v,\varphi,P,Aer^i,U_{H_2O})$$

$$+Tr^i_{atm}(\theta_s,\theta_v,P,Aer^i)\frac{\rho_s}{1-S^i_{atm}(P,Aer^i)\rho_s}Tg^i_{H_2O}(m,U_{U_{H_2O}})] \quad (1)$$

$$Aer^i = (\tau^i_A,\omega^i_0,P^i_A)$$

where (dropping the spectral dependence i)

ρ_{TOA} is the reflectance at the top of the atmosphere,
Tg is the gaseous transmittance by water vapor, Tg_{H_2O}, by ozone, Tg_{O_3}, or other gases, Tg_{OG} (e.g. CO_2, O_2, CH4)
Aer refers to the aerosol model optical properties,
ρ_{atm} is the atmosphere intrinsic reflectance,
Tr_{atm} is the total atmosphere transmission (downward and upward)
S_{atm} is the atmosphere spherical albedo,
ρ_S is the surface reflectance to be retrieved by the atmospheric correction procedure,

The geometrical conditions are given by θ_s, the solar zenith angle, θ_v, the view zenith angle and ϕ, the difference between the solar and view azimuth angle,

P is the pressure in Millibars, which influences the amount of molecules in the atmosphere and the concentration of absorbing gases,

τ_A, ω_0 and P_A describe the aerosol properties in band i.
τ_A is the spectral aerosol optical thickness,
ω_0 is the spectral aerosol single scattering albedo, describing the absorption of the aerosol, ω_0 is equal to 1 for non-absorption particles and to 0 for completely absorbing aerosol,
P_A is the spectral aerosol phase function,

U_{H_2O} is the integrated water vapor content in centimeters
U_{O_3} is the integrated columnar ozone content in cm-atm
m is the air-mass computed as $1/\cos(\theta_s)+1/\cos(\theta_v)$

The water vapor affect on the atmosphere intrinsic reflectance is approximated in 6S as:

$$\rho^i_{atm}(\theta_s,\theta_v,\phi,P,Aer^i,U_{H_2O}) = \rho^i_R(\theta_s,\theta_v,\phi,P) + \left(\rho^i_{R+Aer}(\theta_s,\theta_v,\phi,P,Aer^i) - \rho^i_R(\theta_s,\theta_v,\phi,P)\right)Tg^i_{H_2O}(m,\frac{U_{U_{H_2O}}}{2}) \qquad (2)$$

where ρ_R represents the atmospheric reflectance due to molecular (Rayleigh) scattering, and ρ_{R+Aer} represents the reflectance of the combined molecular and aerosol components, which is computed in 6S using the successive order of scattering method, and thereby accounting correctly for the so-called coupling effect (Deschamps *et al*., 1983). This approximation conserves the correct computation of the coupling, and supposes that the water vapor is mixed with aerosol and that the molecular scattering is not affected by the water vapor absorption. This approximation is reasonable in most cases where observation bands are narrow and outside the water vapor strong absorption as it is the case for VIIRS or MODIS.

The total atmosphere transmission, T_r, is further decomposed into downward and upward terms, which are respectively dependent on θ_s and θ_v and are computed using the same function by virtue of the reciprocity principle, that is:

$$Tr^i_{atm}(\theta_s,\theta_v,P,Aer^i) = T^i_{atm}(\theta_s,P,Aer^i)T^i_{atm}(\theta_v,P,Aer^i) \qquad (3)$$

2.2.2.2 Lambertian infinite target correction implementation

In the implementation of the algorithm, functions related to atmospheric scattering and absorption, ρ_{atm}, T_{atm} and S_{atm} are interpolated from pre-computed look up table since they cannot be simply modeled. On the other hand, the gaseous transmission functions can be written as simple analytical expressions. The molecular reflectance term can be computed very efficiently using a semi-empirical approach based on the decomposition suggested by Chandrasekhar.

Using the approximation given below in (4), the dependence on the atmospheric pressure can be accounted for, by only computing ρ_{R+Aer} at standard pressure, P_0, which substantially reduces the dimension of the look-up tables. We use:

$$\rho^i_{atm}(\theta_s,\theta_v,\phi,P,Aer^i,U_{H_2O}) = \rho^i_R(\theta_s,\theta_v,\phi,P) + \left(\rho^i_{R+Aer}(\theta_s,\theta_v,\phi,P_0,Aer^i) - \rho^i_R(\theta_s,\theta_v,\phi,P_0)\right)Tg^i_{H_2O}(m,\frac{U_{U_{H_2O}}}{2}) \qquad (4)$$

A similar approach is applied to the atmospheric transmission term, that is:

$$T_{atm}^{i}(\theta,P,Aer^{i}) = T_{atm}^{i}(\theta,P_0,Aer^{i})\frac{T_R^{i}(\theta,P)}{T_R^{i}(\theta,P_0)} \qquad (5)$$

where T_R is the atmosphere transmission function due to molecule.

2.2.2.3 Lambertian infinite target correction operational approach

The code implements Equations (1) through (5), using a look-up table approach and analytic expressions. The following section details the computation of each term in the computer code.

2.2.2.3.1 Gaseous transmission by other gases

The gaseous transmission by gases, other than water vapor or ozone, $Tg_{OG}^{i}(m,P)$, in the VIIRS bands can written as a function of the air mass, m, and the pressure P (in atm), as follows:

$$Tg_{OG}^{i}(m,P) = \exp\left[m\left(a_0^iP + a_1^iLog(P)\right) + Log(m)\left(b_0^iP + b_1^iLog(P)\right) + mLog(m)\left(c_0^iP + c_1^iLog(P)\right)\right] \qquad (6)$$

2.2.2.3.2 Ozone Gaseous transmission

The ozone gaseous transmission, $Tg_{O_3}^{i}(m,U_{O_3})$, in the narrow VIIRS bands (i.e., in the Chappuis band) could be simply modeled as:

$$Tg_{O_3}^{i}(m,U_{O_3}) = e^{-ma_{O_3}^{i}U_{o3}} \qquad (7)$$

The coefficients $a_{O_3}{}^{i}$ are determined by curve fitting. The units of U_{O_3} are cm-atm.

2.2.2.3.3 Water vapor Gaseous transmission

The water vapor transmission, $Tg_{H_2O}^{i}(m,U_{H_2O})$, is modeled as:

$$Tg_{H_2O}^{i}(m,U_{H_2O}) = \exp\left[a_{H_2O}^{i}mU_{H_2O} + b_{H_2O}^{i}Log(mU_{H_2O}) + c_{H_2O}^{i}mU_{H_2O}Log(mU_{H_2O})\right] \qquad (8)$$

The coefficients $a_{H2O}{}^{i}$, $b_{H2O}{}^{i}$ and $c_{H2O}{}^{i}$ are determined by curve fitting.

2.2.2.3.4 Molecular atmospheric reflectance at standard pressure

The molecular atmospheric reflectance at standard pressure, $\rho_R^i(\theta_s, \theta_v, \phi, P_0)$, is computed by the subroutine CHAND.f, which takes as input, the geometry (μ_s, μ_v, Φ), where μ_s (resp. μ_v) is the cosine of the solar (resp. view) zenith angle, and Φ the relative azimuth and the molecular optical thickness in that case at standard pressure, which is pre-computed (by 6S), τ_R.

2.2.2.3.5 Molecular atmospheric reflectance at actual pressure

The molecular atmospheric reflectance at actual pressure adjustment, $\rho_R^i(\theta_s, \theta_v, \phi, P_0)$, is simply done by adjusting the amount of molecule or the molecular optical thickness, according to:

$$\tau_R(P) = P\ \tau_R \tag{9}$$

where the pressure P is expressed in atmospheres.

2.2.2.3.6 Intrinsic reflectance at standard pressure

The intrinsic atmospheric reflectance at standard pressure, $\rho_{R+Aer}^i(\theta_s, \theta_v, \phi, P_0, Aer^i)$, is pre-computed by 6S in a look table for each band and each aerosol model (P_A,ω_0) The step in solar zenith angle is 4 deg, in view angle is 4 deg corresponding to the gauss quadrature of 24 angles (with the nadir added), the step is kept constant in scattering angle (4 degree), Θ , which is defined as:

$$\cos(\Theta) = -\cos(\theta_s)\cos(\theta_v) - \cos(\phi)\sin(\theta_s)\sin(\theta_v)\ , \tag{10}$$

resulting in a variable number of steps for each θ_s, θ_v configuration. The indexing to the correct values in the look up table is achieved through the use of the ANGLE lookup table, which keeps track of the number of geometry computed for each θ_s, θ_v configuration. Though, more expensive and more complicated to interpolate within, this structure achieves a higher precision with a reduced size look up table, for a term whose accuracy is critical to the atmospheric correction.

The step in aerosol optical depth is variable to optimize the performance of the correction with the error induced by the interpolation (i.e. finer a low optical depth).

2.2.2.3.7 Atmospheric transmission on at standard pressure

Atmospheric transmission, $T_{atm}^i(\theta, P_0, Aer^i)$, is pre-computed using 6S, with the successive order of scattering method assuming the bottom of the layer is illuminated with isotropic light.

The code accounts for the mixing aerosol molecule within the atmosphere. The values are computed with a step of 4 deg in θ and for each aerosol model and each band for the predefined values of τ_A. The interpolation for any θ and τ is relatively straightforward since this table has only 2 dimensions. The table volume is also very modest.

2.2.2.3.8 Molecular (Rayleigh) transmission at standard pressure

The molecular transmission, $T_R^i(\theta, P_0)$, at standard pressure is computed using the value of molecular optical depth at standard pressure, τ_R. Using the two stream method, the molecular transmission is approximated by:

$$T_R^i(\theta, P_0) = \frac{\left\lfloor \frac{2}{3} + \cos(\theta) \right\rfloor + \left\lfloor \frac{2}{3} - \cos(\theta) \right\rfloor e^{-\tau_R / \cos(\theta)}}{\frac{4}{3} + \tau_R} \qquad (11)$$

2.2.2.3.9 Molecular (Rayleigh) transmission at actual pressure.

The Rayleigh transmission, $T_R^i(\theta, P)$, determination uses the same method as in Section 3.4.2.3.5 we simply replace τ_R in Equation (9) with $\tau_R(P)$.

2.2.2.3.10 Atmosphere spherical albedo at actual pressure

The atmospheric spherical albedo at actual pressure, $S_{atm}^i(P, Aer^i)$, is defined as:

$$S_{atm}^i(P, Aer^i) = \int_0^{\pi/2}\int_0^{\pi/2}\int_0^{2\pi} \rho_{atm}^i(\theta, \theta', \phi, P, Aer^i)\sin(\theta)\cos(\theta')\,d\theta d\theta' d\phi \qquad (12)$$

By ignoring the water vapor dependence on the atmosphere intrinsic reflectance (S acting as a second order effect), we can write the same relation we have written for the atmosphere intrinsic reflectance, that is

$$S_{atm}^i(P, Aer^i) = (S_{atm}^i(P_0, Aer^i) - S_R^i(P_0)) + S_R^i(P) \qquad (13)$$

So the $S_{atm}^i(P_0, Aer^i)$ is stored in a pre-calculated look up table depending only on aerosol optical depth and model. The $S_R^i(P)$ term is computed by an analytic expression based on the integral of Equation (11) that is:

$$S_R^i(P) = \sum_j a_j EXPI(\tau_R, n) \qquad (14)$$

where EXPI is the exponential integral function (see 6S code for details; Vermote et al., 1994).

2.2.3. Adjacency Adjustment

2.2.3.1.Formalism

If the target is of infinite dimension, the equation of transfer (here rewritten without gaseous absorption to simplify the writing), and dropping the spectral dependence then:

$$\rho_{toa} = \rho_{R+Aer} + \frac{T_{R+Aer}(\theta_s)T_{R+Aer}(\theta_v)\rho_s}{1 - S_{R+Aer}\rho_s} \quad (15)$$

In the case where the target is not infinite, Equation (15) becomes:

$$\rho_{toa} = \rho_{R+Aer} + \frac{T_{R+Aer}(\theta_s)}{1 - S_{R+Aer}\rho_e}\left(e^{-\tau/\mu_v}\rho_s + t^d_{R+Aer}(\theta_v)\rho_e\right) \quad (16)$$

$$\rho_e = \frac{1}{2\pi}\int_0^{2\pi}\int_0^{\infty}\rho(r,\psi)\frac{dF(r)}{dr}dr\,d\psi \quad (17a)$$

In Equation (16), the downward transmission, $T_{R+Aer}(\theta_s)$, where θ_s refers to the solar zenith angle, and the upward transmission, $T_{R+Aer}(\theta_v)$, where θ_v refers to view zenith angle are considered separately. Furthermore, the upward transmission term, $T_{R+Aer}(\theta_v)$, is decomposed into two parts: (a) the diffuse upward transmission $t^d_{R+Aer}(\theta_v)$, and (b) the direct upward transmission ($e^{-\tau/\mu v}$), (where μ_v refers to the cosine of the view zenith angle and τ refers to the atmosphere optical thickness). In extenso, we have

$$T_{R+Aer}(\theta) = t^d_{R+Aer}(\theta) + e^{-\tau_{R+A}/\mu} \quad (17b)$$

By decomposing the signal in this way the contribution coming directly from the target the term ($e^{-\tau/\mu_v}\rho_s$) is isolated from the “environment contribution”, ρ_e, coming from adjacent pixels not in the direct line of sight. The adjacent pixels contribute to the signal due to the atmospheric scattering of the photons toward the sensor and their contribution is therefore weighted by the diffuse upward transmission.

The effective “reflectance” of the environment, r_e, is not a simple average of the pixel around the target but is the result of the convolution of the atmospheric point spread function dF(r)/dr by the two dimensional surface reflectance values. In Equation (17), the spatial coordinate system used is the polar coordinate system (r for radius, $\Psi$for angle), which is very convenient since in most cases the point spread function is only dependent the distanced from the target and not the angle. In practice the dependence with respect to $\Psi$is actually dropped.

The atmospheric point spread functions for molecules and aerosols have been computed using Monte-Carlo computation and fitted using empirical functions and are available in the 6S code (Vermote et al., 1997). Figure 3 shows the environment function for molecules and aerosols as a function of the distance from the target center for nadir viewing condition and for a sensor located at the top of the atmosphere. In the aerosol case, the contribution of the environment decreases quickly with distance. In the case of molecules, scattering is more important, the contribution of the environment varies more slowly, and the impact of the environment can be seen at larger distances. It is worth pointing out that these environment functions will vary as a function of view angle and altitude of the sensor within the atmosphere (Vermote et al., 1997), and also, to a certain extent, will depend on the aerosol type (especially their vertical profile).

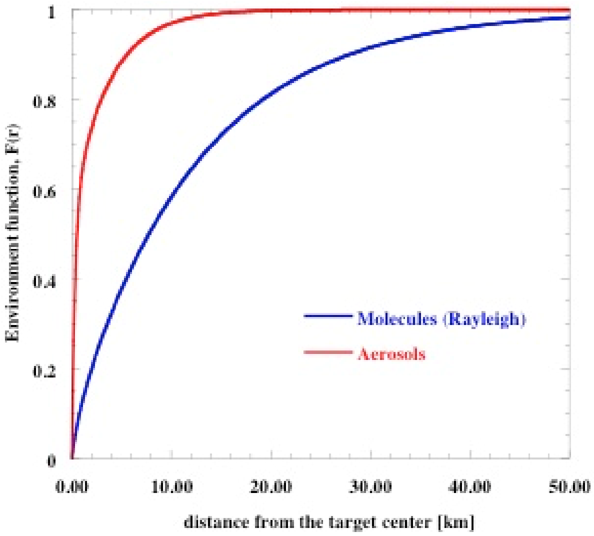

Figure 3: Atmospheric environment function as a function of the distance from the target center, for molecules and aerosols.

In practice, the atmosphere environment function, F(r), is computed by a weighting average of the individual molecules and aerosol environment functions using their respective upward diffuse transmissions,($t_d^R(\theta_v)$ and $t_d^{Aer}(\theta_v)$), that is:

$$F(r) = \frac{t_d^R(\theta_v)F^R(r) + t_d^{Aer}(\theta_v)F^A(r)}{t_d^{R+Aer}(\theta_v)} \tag{18}$$

2.2.3.2. Correction for adjacency effect-implementation

In the Lambertian approxiamtion, Equation (15) shows that the surface reflectance, ρLamb can be retrieved in two simple steps given in Equation (19a) and (19b):

$$\gamma = \frac{\rho_{toa} - \rho_{R+Aer}}{T_{R+Aer}(\theta_s)T_{R+Aer}(\theta_v)} \tag{19a}$$

$$\rho_{Lamb} = \frac{\gamma}{1 + S_{R+Aer}\gamma} \tag{19b}$$

If the target is not of infinite radius then the result of Equation (19a), becomes,

$$\gamma = \frac{\rho_s e^{-\tau/\mu_v} + t^d_{R+Aer}(\theta_v)\rho_e}{T_{R+Aer}(\theta_v)(1 - S_{R+Aer}\rho_e)} \tag{20}$$

which can easily be solved for ρs:

$$\rho_s = [\gamma T_{R+Aer}(\theta_v)(1 - S_{R+Aer}\rho_e) - t^d_{R+Aer}(\theta_v)\rho_e]/e^{-\tau/\mu_v} \tag{21}$$

Since the Lambertian surface reflectance is computed before the adjacency correction (an average of the lambertian correction is needed in the adjacency correction) ρLamb can be used instead of γ to compute ρs. This results in the following correction formula:

$$\rho_s = [\frac{(1 - S_{R+Aer}\rho_e)}{(1 - S_{R+Aer}\rho_{Lamb})} T_{R+Aer}(\theta_v)\rho_{Lamb} - t^d_{R+Aer}(\theta_v)\rho_e]/e^{-\tau/\mu_v} \tag{22}$$

To compute re it is necessary to convolve the atmospheric point spread function with the two dimensional surface reflectance according to Equation (17a). The actual surface reflectance at a very fine scale level is usually not available; instead the actual measurements can be used. An approximation for Equation (17) (Putsay, 1992) is:

$$\rho_e = \sum_{j=-n}^{n}\sum_{i=-n}^{n} \frac{dF(r(i,j))}{dr}\rho_{Lamb}(i,j) \tag{23}$$

In Equation (23), the pixels of the image itself are used to compute the background reflectance, therefore the average point spread function at the pixel location (i,j) is used. The second approximation is that the estimate of the surface reflectance at location (i,j) using the infinite radius target approximation is used instead of the actual reflectance. That provides a first guess for the environment contribution that may actually be refined by successive iterations, but those iterations are usually not necessary (Putsay, 1992).

This first guess is based on the order of tens to hundreds of pixels, which according to the MODIS surface reflectance ATBD corresponds to an n between 3 and 10. In practice, the contribution from the environment encompasses the pixels within 1200 m of the center pixel. The VIIRS algorithm uses n=3 for the imagery band values and n=2 for the moderate resolution band values.

2.3.3.3.Correction for adjacency effect-operational approach

Most of the term described in Equations (19) to (22) are already in look up table. The additional look up table that needs to be provided is the computation of the optical thickness at the given wavelenght, τ_{R+A}, used to compute the direct transmission term, $e^{-\tau_{R+A}/\mu_v}$, this optical thickness, $\tau_{R+A}=\tau_A+\tau_R$ is computed from the spectral extinction coefficient stored in the spherical albedo look up table to compute τ_A□ and the molecular optical thickness τ_R. The atmospheric point spread function is also stored as a look up table for the Rayleigh, $dF_R(r)/dr$ and aerosol contribution $dF_A(r)/dr$.

2.2.4 BRDF atmosphere coupling correction

2.2.4.1. Formalism

Equation (15) assumed that the target is lambertian, if we account for the fact that it is not a lambertian reflector, Equation (15) can be written as (Vermote, 1997)

$$\rho_{toa}(\mu_s,\mu_v,\varphi)=\rho_{R+Aer}(\mu_s,\mu_v,\varphi)+e^{-\tau/\mu_s}e^{-\tau/\mu_v}\rho_s(\mu_s,\mu_v,\varphi)+e^{-\tau/\mu_v}t_d(\mu_s)\overline{\rho}_s+e^{-\tau/\mu_s}t_d(\mu_v)\overline{\rho}'_s+ t_d(\mu_v)t_d(\mu_s)\overline{\overline{\rho}}_s+\frac{T_{R+Aer}(\mu_s)T_{R+Aer}(\mu_v)S_{R+A}\left(\overline{\overline{\rho}}_s\right)^2}{1-S_{R+Aer}\overline{\overline{\rho}}_s} \qquad (23a)$$

with μ_s (resp. μ_v) the cosine of the sun (resp. view) zenith angle, ϕ the relative azimuth (sun – view), $\overline{\rho}_s$, $\overline{\rho}'_s$, and $\overline{\overline{\rho}}_s$ the term accounting for the coupling between the atmosphere and the surface BRDF, if the target is lambertian then $\overline{\rho}_s=\overline{\rho}'_s=\overline{\overline{\rho}}_s=r_s$; otherwise we have:

$$\overline{\rho}_s(\mu_s,\mu_v,\phi)=\frac{\int_0^{2\pi}\int_0^1 \mu L^{\downarrow}_{R+A}(\mu_s,\mu,\phi')\rho_s(\mu,\mu_v,\phi'-\phi)d\mu d\phi'}{\int_0^{2\pi}\int_0^1 \mu L^{\downarrow}_{R+A}(\mu_s,\mu,\phi')d\mu d\phi'} \qquad (23b)$$

$$\overline{\rho}'_s(\mu_s,\mu_v,\phi)=\overline{\rho}_s(\mu_v,\mu_s,\phi) \qquad (23c)$$

$$\overline{\overline{\rho}}_s(\mu_s,\mu_v,\phi)=\overline{\overline{\rho}'_s(\mu_s,\mu_v,\phi)} \qquad (23d)$$

Where $L^{\downarrow}_{R+A}(\mu_s,\mu,\phi')$ is the downwelling flux.
Equation (23d) is approximated like the spherical albedo or white sky albedo, namely:

$$\bar{\bar{\rho}}_s \cong \int_0^1 \int_0^{2\pi} \int_0^1 \mu \rho_s(\mu,\mu,\phi'-\phi)\,d\mu\, d\phi'\, d\mu' \tag{23e}$$

2.2.4.2. BRDF atmosphere coupling correction Implementation

The BDRF of the target, $\rho_s(\mu,\mu',\phi')$ is in general unknown for any geometrical condition for the purpose of atmospheric correction. However, we will assume that the BRDF shape can be determined a priori. This simplifying assumption is necessary since Equation (23a) shows that the Top of the Atmosphere reflectance is given in terms of integrals of the BRDF of the surface Equations (23b-e). In other words Equation (23a) is a non-linear integral equation for the BRDF function. Solving this equation rigorously in an operational setting is prohibitive since it would require multiple iterations of a radiative transfer model.

The unknown reflectance is the line of sight reflectance $\rho_s(\mu_s,\mu_v,\phi)$ but the BRDF of the target $\rho_s(\mu,\mu',\phi')$ is assumed to satisfy:

$$\rho_s(\mu,\mu',\phi') = \rho_s(\mu_s,\mu_v,\phi)\frac{\rho_m(\mu,\mu',\phi')}{\rho_m(\mu_s,\mu_v,\phi)} \tag{24a}$$

Where $\rho_m(\mu,\mu',\phi')$ is the “modeled” BRDF and the ratio $\frac{\rho_m(\mu,\mu',\phi')}{\rho_m(\mu_s,\mu_v,\phi)}$ is the BDRF shape.

Using that assumption, Equation (23b) can be rewritten as:

$$\bar{\rho}_s(\mu_s,\mu_v,\phi) = \frac{\rho_s(\mu_s,\mu_v,\phi)}{\rho_m(\mu_s,\mu_v,\phi)}\bar{\rho}_m(\mu_s,\mu_v,\phi) = \rho_s(\mu_s,\mu_v,\phi)\bar{\rho}_m^{shape}(\mu_s,\mu_v,\phi) \tag{24b}$$

And similarly for Equations (23c) and (23e):

$$\bar{\rho}'_s(\mu_s,\mu_v,\phi) = \frac{\rho_s(\mu_s,\mu_v,\phi)}{\rho_m(\mu_s,\mu_v,\phi)}\bar{\rho}_m(\mu_v,\mu_s,\phi) = \rho_s(\mu_s,\mu_v,\phi)\bar{\rho}'^{shape}_m(\mu_s,\mu_v,\phi) \tag{24c}$$

$$\bar{\bar{\rho}}_s \cong \frac{\rho_s(\mu_s,\mu_v,\phi)}{\rho_m(\mu_s,\mu_v,\phi)}\int_0^1 \int_0^{2\pi} \int_0^1 \mu \rho_m(\mu,\mu',\phi'-\phi)\,d\mu\, d\phi'\, d\mu' = \rho_s(\mu_s,\mu_v,\phi)\overline{\overline{\rho_m^{shape}}}(\mu_s,\mu_v,\phi) \tag{24d}$$

So Equation (23a) is written as:

$$\rho_{toa}(\mu_s,\mu_v,\phi)=\rho_{R+Aer}(\mu_s,\mu_v,\phi)+\rho_s(\mu_s,\mu_v,\phi)[e^{-\tau/\mu_s}e^{-\tau/\mu_v}+e^{-\tau/\mu_s}t_d(\mu_v)\overline{\rho}_m^{shape}$$

$$+e^{-\tau/\mu_s}t_d(\mu_v)\overline{\rho}'^{shape}_m+t_d(\mu_v)t_d(\mu_s)\overline{\overline{\rho_m^{shape}}}]+\rho_s(\mu_s,\mu_v,\phi)^2\frac{T_{R+Aer}(\mu_s)T_{R+Aer}(\mu_v)S_{R+Aer}\overline{\overline{\rho_m^{shape}}}^2}{1-S_{R+Aer}\overline{\overline{\rho_m^{shape}}}} \tag{25}$$

Equation (25) is a quadratic equation in $\rho_s(\mu_s,\mu_v,\phi)$ that has only one positive solution, since the product of the roots is negative. Therefore solving for $\rho_s(\mu_s,\mu_v,\phi)$ is straightforward once each other term of Equation (25) is computed. The computation of $\overline{\rho}_m^{shape}$, $\overline{\rho}'^{shape}_m$ and $\overline{\overline{\rho_m^{shape}}}$, which are the only quantities not fully defined in the previous section, is described in the operational approach (next section).

2.2.4.3. BRDF atmosphere coupling correction-operational approach

The model of BRDF used for $\rho_m(\mu,\mu',\phi')$ is the operational model used for MODIS Albedo/BRDF product the LiSparse-Reciprocal (LSR), RossThick (RT) linear kernel model that is written as:

$$\rho_m(\mu_s,\mu_v,\phi)=P_1+P_2K_{LSR}(\mu_s,\mu_v,\phi)+P_3K_{RT}(\mu_s,\mu_v,\phi) \tag{26}$$

where

$$K_{RT}(\mu_s,\mu_v,\phi)=\frac{(\pi/2-\xi)\cos\xi+\sin\xi}{\mu_s+\mu_v}-\frac{\pi}{4}$$

$$\cos\xi=\mu_s\mu_v+\sqrt{1-\mu_s{}^2}\sqrt{1-\mu_v{}^2}\cos\phi$$

$$K_{LSR}(\mu_s,\mu_v,\phi)=O(\mu_s,\mu_v,\phi)-\frac{1}{\mu_s}-\frac{1}{\mu_v}+\frac{1}{2}(1+\cos\xi)\frac{1}{\mu_s}\frac{1}{\mu_v}$$

$$O(\mu_s,\mu_v,\phi)=\frac{1}{\pi}(t-\sin t\cos t)(\frac{1}{\mu_s}+\frac{1}{\mu_v})$$

$$\cos t=\frac{h}{b}\frac{\sqrt{D^2+(\tan\theta'\tan\vartheta'\sin\phi)^2}}{\sec\theta'+\sec\vartheta'}$$

$$D=\sqrt{\tan^2\theta'+\tan^2\vartheta'-2\tan\theta'\tan\vartheta'\cos\phi}$$

$$\theta' = \tan^{-1}(\frac{b}{r}\tan\theta_s) \qquad \vartheta' = \tan^{-1}(\frac{b}{r}\tan\vartheta_v)$$

where, h describes the crown model central height above the ground, r and b describe the vertical and horizontal dimensions of the crown spheroid.

The interesting properties of this BRDF model are that the geometrical conditions are decoupled from the surface weighting parameters, therefore:

$$\overline{\rho}_m^{shape}(\mu_s,\mu_v,\phi) = \frac{1+\frac{P_2}{P_1}\overline{K}_{LSR}(\mu_s,\mu_v,\phi)+\frac{P_3}{P_1}\overline{K}_{RT}(\mu_s,\mu_v,\phi)}{1+\frac{P_2}{P_1}K_{LSR}(\mu_s,\mu_v,\phi)+\frac{P_3}{P_1}K_{RT}(\mu_s,\mu_v,\phi)} \qquad (27)$$

So by pre-computing the downward irradiance integrals $\overline{K}_{LSR}(\mu_s,\mu_v,\phi)$ and $\overline{K}_{RT}(\mu_s,\mu_v,\phi)$ for the kernels, $K_{LSR}(\mu_s,\mu_v,\phi)$ and $K_{RT}(\mu_s,\mu_v,\phi)$ storing them in look up tables (they are function of the band i, the optical thickness at 550nm, and the aerosol model), the functions $\overline{\rho}_m^{shape}(\mu_s,\mu_v,\phi)$ and their associate ($\overline{\rho}_m^{'shape}(\mu_s,\mu_v,\phi)$ and $\overline{\overline{\rho}}_m^{shape}$) can be recomputed on the fly. The only unknown at this point is the weight of the BRDF shape function, $P_2^{'} = \frac{P_2}{P_1}$ and $P_3^{'} = \frac{P_3}{P_1}$

Some experiments with MODIS data have shown that the BRDF shape parameter can be fitted as a function of NDVI. That is, to a first order, for low NDVI, low vegetation cover, P'$_2$ and P'$_3$ are expected to be near zero since the BDRF effect are small, for higher NDVI, the coefficient are expected to be higher. It should be noted, that P'$_2$ and P'$_3$ depend on the band as well. In the present version of the code, a linear interpolation is performed between a semi-arid case (low NDVI) and a forest case (high NDVI) for which the P'$_2$ are P'$_3$ have inverted using as large a data record as possible. Figure 4, shows the coefficients. P'$_2$ (Li Sparse Reciprocal) and P'$_3$ (Ross Thick) for three different biomass cases (low, average, high) for each of the VIIRS bands.

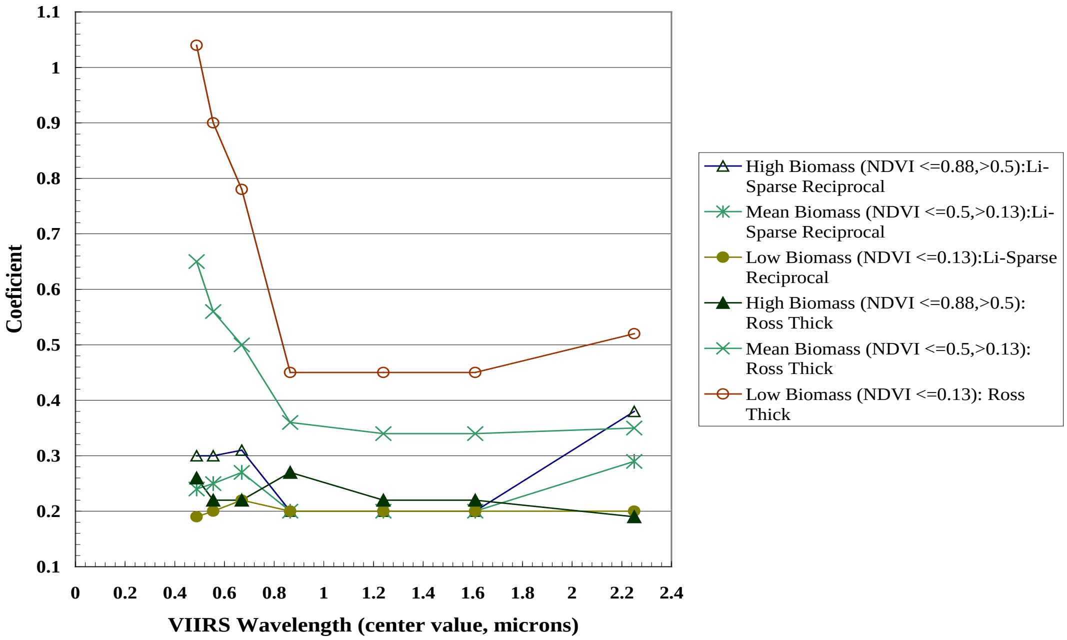

Figure 4. Relationship between BRDF shape and NDVI.

2.2.5 Thin Cirrus Correction

Should thin cirrus (presently defined to possess optical thickness at 640 nm ranging up to 1) be present, the Surface Reflectance EDR and downstream products are generated, with an associated flag in the Land Quality Flag output. The baseline approach for removing much of the thin cirrus-laden pixels is very simple. It assumes that cirrus reflectance is not spectrally dependent, and that cirrus reflectance is spatially homogeneous. This allows the application of a threshold adjustment to all VIIRS bands in the general form

$$\rho_\lambda = \rho_\lambda - (\rho_{1.38}/T^{1.38}_{H20}) \qquad (28)$$

where r_l is the reflectance at the particular band, $\rho_{1.38}$ is the reflectance at the 1.38 micron VIIRS band, and $T^{1.38}{}_{H20}$ is the total two-way transmittance of water vapor at 1.38 microns for the given solar and viewing geometry. $T^{1.38}{}_{H20}$ is assumed to be 0.6, based on Vermote and Vermeulen (1999).

This correction will be applied to the radiances in the other VIIRS reflective bands prior to the application of the lambertian correction. The inherent assumption within Equation (16), even at VIIRS scale, may not be valid under every circumstance, but suspected pixels are nonetheless flagged. A few reasons why the assumption might not be valid include, cirrus ice crystals are not spatially homogeneous, and cirrus adjacency issues. Vermote and Vermeulen (1999) provide additional insights.

2.3. Algorithm Input

The input data sets used by the VIIRS SR algorithm are listed in Tables 2-1 and 2-2. All dynamic input data derived from VIIRS SDR Level 1 files are used in their original swath projection format. All radiance and reflectance data correspond to the calibrated top-of-atmosphere (at-sensor) values.

Table 2-1: List of dynamic input data sets used in the VIIRS SR algorithm.

Input	Data Sets
VIIRS Imagery Band Geolocation Data	• Latitude • Longitude • Satellite Azimuth Angle • Satellite Zenith Angle • Solar Azimuth Angle • Solar Zenith Angle • Satellite Range • Quality Flag
VIIRS Imagery Band Data	• Channel I1 radiance • Channel I2 radiance • Channel I3 radiance • Quality Flag
VIIRS Moderate Band Geolocation Data	• Latitude • Longitude • Satellite Azimuth Angle • Satellite Zenith Angle • Solar Azimuth Angle • Solar Zenith Angle • Satellite Range • Quality Flag
VIIRS Moderate Band Data	• Channel M1 radiance • Channel M2 radiance • Channel M3 radiance • Channel M4 radiance • Channel M5 radiance • Channel M7 radiance • Channel M8 radiance • Channel M10 radiance • Channel M11 radiance • Quality Flag
Aerosol Data	• Aerosol Model • Aerosol Optical Depth • QF1/2/3/4/5 (quality flags) • Angstrom Exponent 1
VIIRS Cloud Mask	• VIIRS Cloud Mask product
GFS Input Data	• Total Column Ozone • Total Precipitable Water • Surface Pressure
Cloud Height Data	• Shadow Mask

Table 2-2: List of input look-up tables used in the VIIRS SR algorithm.

Input	Data Sets
Aerosol Optical Thickness	• Table of 20 aerosol optical thicknesses.
Viewing Zenith Angles	• Table of 40 viewing zenith angles •
Solar Zenith Angles	• Table of 38 solar zenith angles
Scattering Angle Increment	• Scattering Angle Increment (1 value)
Scattering Angle	• Location of the first (maximum) scattering angle corresponding to a pair of solar/sensor zenith angles (105 values
Physical Ranges and Coefficients	• Min/Max for Retrieved Surface Reflectance • Min/Max for Aerosol Optical Depth • Minimum value for GFS water vapor, ozone, surface pressure • Aerosol Min/Max Model Values • Rayleigh Optical Depth • Ozone (1 value), water vapor (3 values), and other gas (6 values) transmittance coefficients.
Reflectivities	Table of reflectivities, one value each for combinations of: • 4 aerosol models • 20 AOT values (from aot) • 10 land channels: • M(1,2,3,4,5,6,7,8,10,11) • 5527 scattering angle combinations
Transmittances	Table of transmittances, one value each for combinations of: - 4 aerosol models - 20 AOT values (from aot) - 10 land channels: M(1,2,3,4,5,6,7,8,10,11) - 15 solar zenith angle bins
Albedos	Table of albedos, one value each for combinations of: - 4 aerosol models - 20 AOT values (from aot) - 10 land channels: M(1,2,3,4,5,6,7,8,10,11)

2.4. Algorithm Output

The input data sets used by the VIIRS SR algorithm are listed in Table 2-3.

Table 2-3: VIIRS SR output science data sets.

Data Set Name	Description	Dimension
Surface Reflectances for Imagery Channels	Surface Reflectances for Channels: I1, I2, I3 (Integer)	[1536x6400]
Quality Flags for Imagery Channels	Quality Flags: QF1, QF2, QF3, QF4, QF5, QF6, QF7	[1536x6400]
Surface Reflectances for Moderate Channels	Surface Reflectances for Channels: M1,M2,M3,M4,M5,M7,M8,M10,M11	[768x3200]

Quality Flags for Imagery Channels	Quality Flags: QF1, QF2, QF3, QF4, QF5, QF6, QF7	[768x3200]

2.5. Performance Estimates

The Surface Reflectance EDR algorithm performance may be affected by sensor, solar and viewing geometry including target elevation above sea level, atmospheric, adjacency, and coupling of the atmosphere and surface effects, i.e. BRDF, among others. The atmospheric effects include aerosol and Rayleigh scattering, gaseous absorption, and thermodynamic conditions. The largest atmospheric effects on surface reflectance retrieval are from variations in aerosol properties. Sensor calibration is the primary contributor to sensor effects.

Validation requires detailed knowledge of the relationship between processes and variables that may be used to monitor those processes over the full range of natural conditions. Post-launch activities include refinement of algorithms and uncertainty estimates based on near-direct comparisons with correlative data and selected, controlled analyses.

2.5.1 AOT validation

One key point about surface reflectance validation is the validation of the retrieved atmospheric condition (i.e. aerosol optical depth). For that purpose, we will use the AERONET network to validate the aerosol optical thickness. **As an example**, we show Figure 5 the evaluation of the MODIS collection 6 aerosol over land conducted over the several sites selected in (Lyapustin et al., 2011), a collection of “dark” and “brighter” sites that enables to test the limit of the inversion. The analysis is done by averaging the 1km aerosol retrievals over a subset of 11x11 pixels centered on the AERONET instrument location, cloud, snow and water are excluded in the averaging but no other particular filtering is done (i.e. MOD04 and MAIAC exclude some of the highest or lowest AOT retrieval before averaging). The results are presented in Figure 5 for the East Coast sites selection (GSFC, Stennis, Walker Branch and Wallops). The results are extremely similar both in slope and correlation to those presented in (Lyapustin et al., 2011), and even show better correlation (0.88 versus 0.66) and lower intercept (0.04 versus 0.13) for the Solar Village site (not shown) that is particularly challenging in term of aerosol retrieval. Note that the bias in optical thickness is compensated to some extend in the atmospheric correction process where the same model is used for the inversion and the correction.

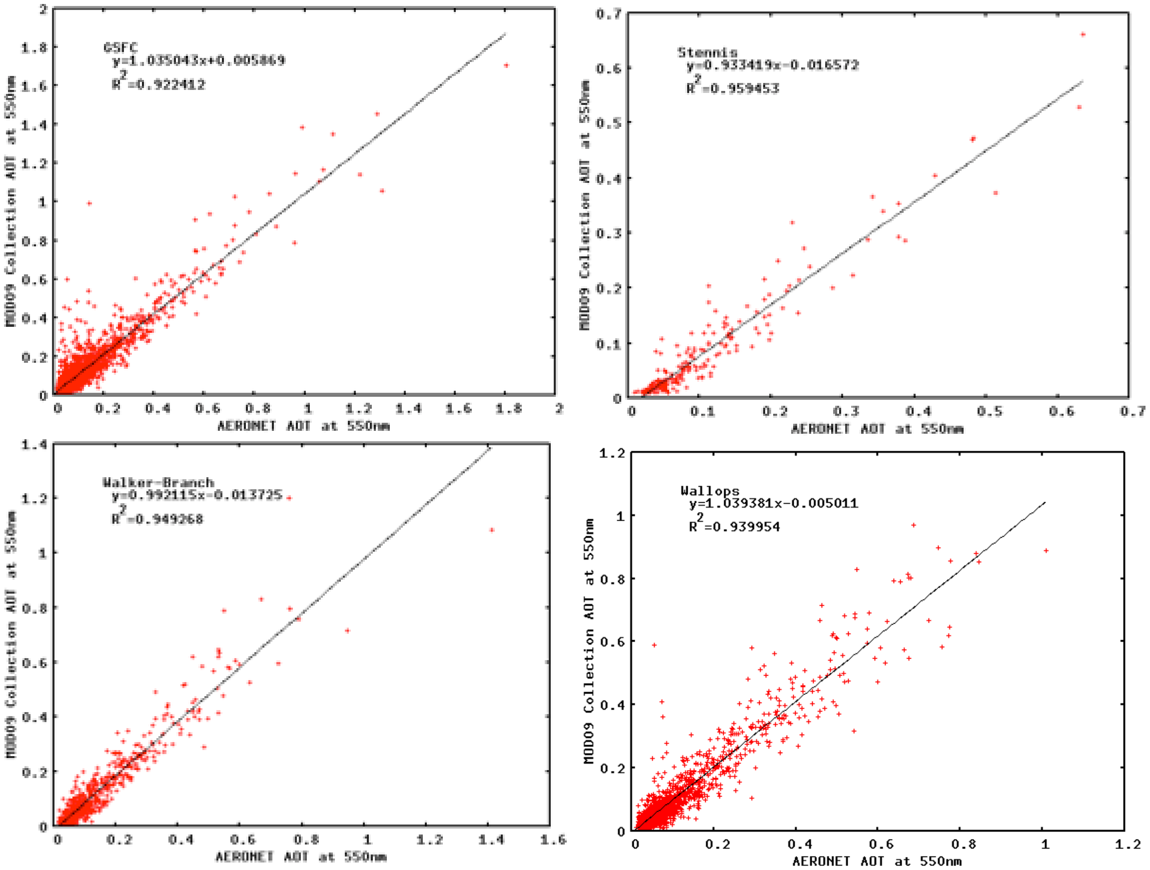

Figure 5: Scatterplot of the MOD09 AOT at 550nm versus le AERONET AOT at 550nm for East Coast sites selection, GSFC (top left), Stennis (top right), Walker Branch (bottom left) and Wallops (bottom right).

2.5.2 Surface reflectance accuracy assessment

The performance of the surface reflectance product itself has been provisionally quantified using the standard approach developed for MODIS and VIIRS surface reflectance product. The approach uses the AERONET dataset (Dubovik et al, 2002). We also use the 6S radiative transfer code to perform very accurate atmospheric correction of the top of the atmosphere around the AERONET site (9 km x 9 km) and get a reference that can be compared to. The standard performance metrics: accuracy, precision and uncertainty, (Vermote and Kotchenova, 2008) can then be derived from this comparison. Nevertheless, we improved the validation scheme using Dubovik’s approach i.e. the microphysical parameters of aerosol are directly related to the aerosol optical thickness (Dubovik et al., 2002). Now we describe the microphysical parameters of the aerosol i.e. size-distribution ($\%C_f$, r_f, σ_f, $\%C_c$, r_c, σ_c), refractive indexes (n_r, n_i), % of sphericity parameters (%sp) by both the optical thickness and the Angström coefficient. The refinement allows an improved microphysical characterization by 30%. According Roger et al., 2016, Figure 6 gives an example of how we now retrieved the radius of the fine mode with our new method (14% error) for the 230 AERONET sites (Figure 7).

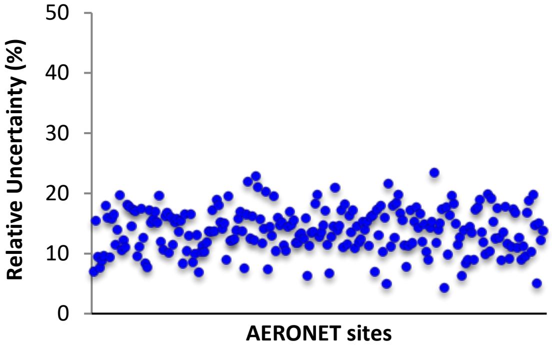

Figure 6: Retrieval of the radius of the fine mode.

Table 2.4 gives the relative percentage of uncertainties on retrieval for all the aerosol microphysical parameters.

Table 2-4: Relative percentage of aerosol microphysical parameters retrieval.

$\%C_f$	r_f	σ_f	$\%C_c$	r_c	σ_c	n_r	n_i	%sp
23%	14%	11%	21%	15%	8%	3%	55%	21%

The resulting global error of this new method in terms of surface reflectance is reported in Figure 8. Thus, we can state that the “reference” defined by the new approach is precise within 1-2%, which is much below the specifications over Land (Roger et al., 2016).

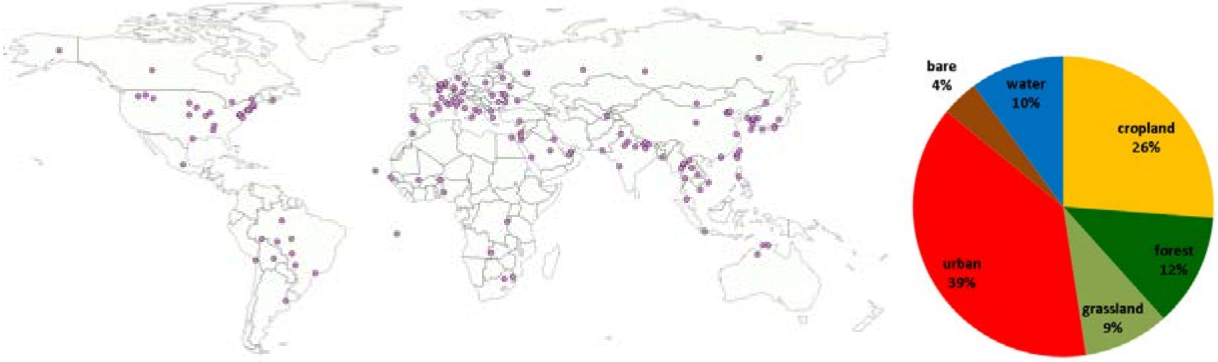

Figure 7: AERONET Sites (left) and the associated Land cover distribution (right) used for SR validation.

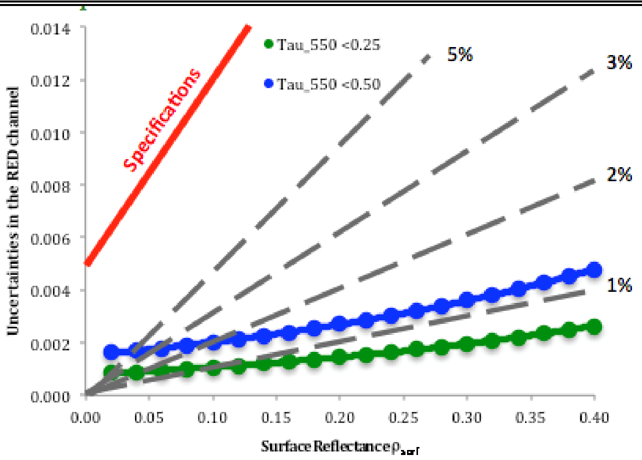

Figure 8: Global error of the surface reflectance (in the red) used as reference for the validation for two aerosol optical thicknesses at 550nm categories.

We apply the method to the validation of VIIRS. First results are illustrated Figure 9 (a) for the Red channel (band M5). For comparison, we show results for MODIS Collection 6 for the equivalent channel (band 1)

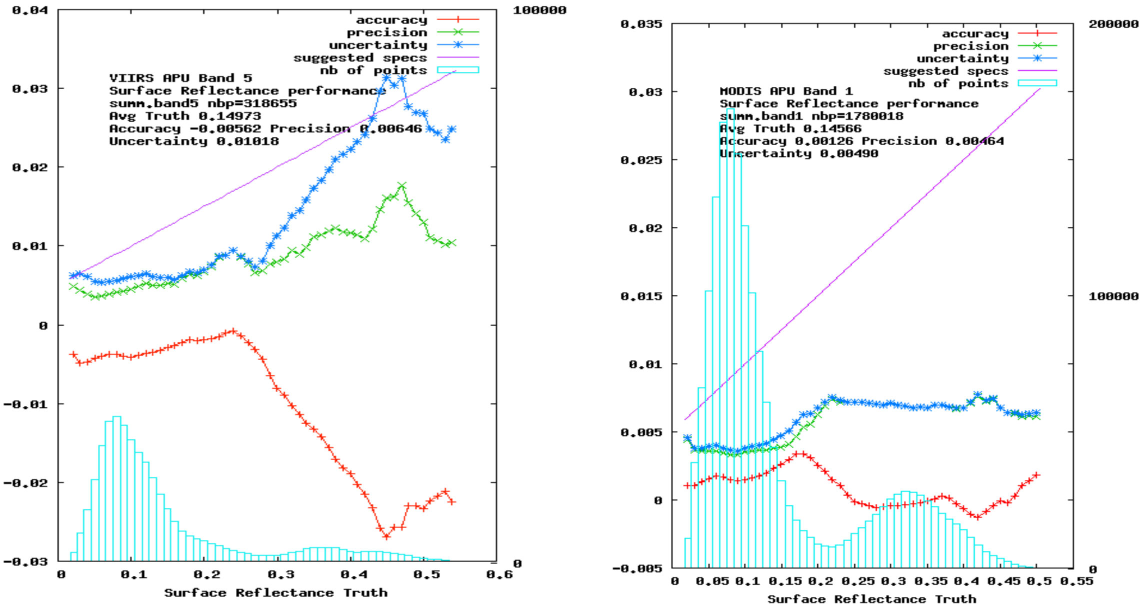

a) b)

Figures 9: Estimates of BRDF corrected surface reflectance for a) first results for VIIRS band M5 (red), and b) MODIS-Terra Band 1 collection 6 (red).

2.5.3 Direct inter-comparison using BELMANIP

Getting a consistent database of surface reflectance necessitates several treatments and generates uncertainties. At the end, we need to check the inter-comparison of the surface reflectance products from different sensors can be used to evaluate their performance and check their inter-consistency. The VIIRS data are accurately calibrated and the directional surface reflectance product has been validated through the various stage defined by the MODIS land validation approach (Morisette et al., 2002). Thus, MODIS directional surface reflectance product can be considered as a good reference to evaluate both AVHRR and VIIRS. However, in order to achieve a precise intercomparison, we need to correct the directional effects by using BRDF corrected surface reflectance as well as adjusting for the spectral bands of the sensors.

As a proof of concept, the VIIRS surface reflectance and Aqua MODIS data over the BELMANIP2 (BEnchmark Land Multisite ANalysis and Intercomparison of Products) sites were intercompared, using the spectral and directional corrections. BELMANIP2 is an updated version of BELMANIP1 (Baret et al., 2006) which was built using sites from existing experimental networks (FLUXNET, AERONET, VALERI, BigFoot) completed with selected sites from the GLC2000 land cover map. The original BELMANIP2 dataset included 420 sites (Figure 10).

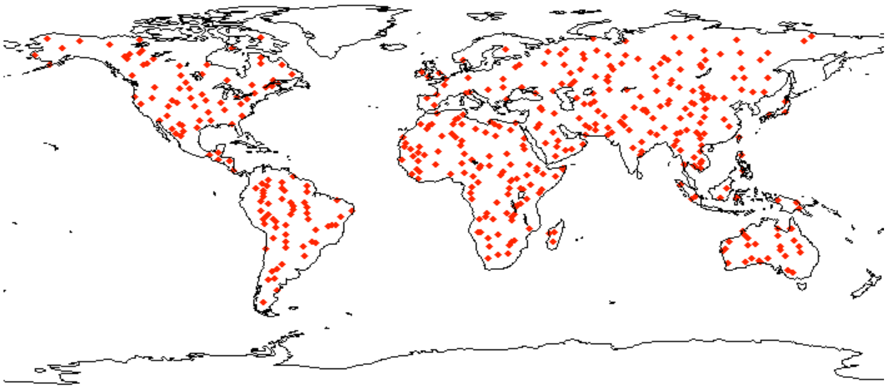

Figure 10. Distribution of the BELMANIP2 sites

Figure 11 shows the first results of the cross comparison of the VIIRS and MODIS Aqua for the BELMANIP2 sites. The plots show that the new processing of VIIRS (C1.1) is in a good agreement with MODIS (left), we also show the continuous monitoring of C1.1 (Right) to ensure stability/consistency.

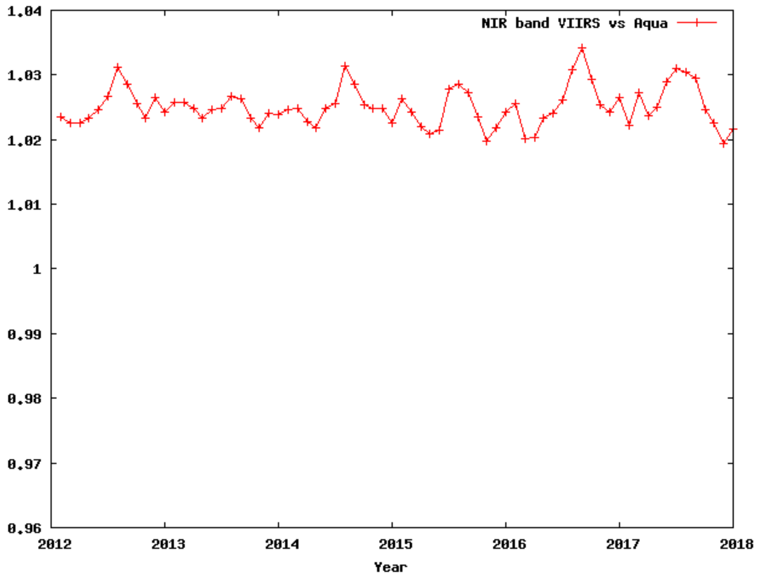

Figure 11. Cross comparison results of the VIIRS and MODIS-Aqua SR product on a monthly basis for the BELMANIP sites reprocessed version (C1.1) for the band M7 (near infrared).

3. ASSUMPTIONS AND LIMITATIONS

3.1. Performance Assumptions

Algorithm performance is dependent on observation conditions and therefore will be degraded when optically thick haze, heavy smoke plumes, volcanic ash etc. are in the line of sight.

3.2. Potential Improvements

Algorithm updates are expected in coordination with the evolving science content of the input NOAA Enterprise EDR products (primarily Cloud Mask and Aerosol ERDs).

4. REFERENCES

List all references to external documents.

Baret, F., Morissette, J., Fernandes, R., Champeaux, J.L., Myneni, R., Chen, J., Plummer, S., Weiss, M., Bacour, C., Garrigues, S. and Nickeson, J.E., 2006. Evaluation of the representativeness of networks of sites for the validation and inter-comparison of land biophysical products. proposition of the CEOS-BELMANIP. IEEE Trans. Geosc. Remote Sens., 44(7): 1794-1803

Becker-Reshef I., Vermote E., Lindeman M., Justice C. 2010. A Generalized Regression-based Model for Forecasting Winter Wheat Yields in Kansas and Ukraine Using MODIS Data. Remote Sensing of Environment, 114, 1312-1323

Berk, A., G. P. Anderson, P. K. Acharya, J. H. Chetwynd, L. S. Bernstein, E. P. Shettle, M. W. Matthew, and S. M. Adler-Golden (1999). *MODTRAN4 User's Manual*. Air Force Research Laboratory, Space Vehicles Directorate, Hanscom AFB, MA 01731-3010.

Franch, B., Vermote, E.F., Becker-Reshef, I., Claverie, M., Huang, J., Zhang, J., Justice, C. and Sobrino, J.A. 2015. Improving timeliness of winter wheat production forecast in United States of America, Ukraine and China using MODIS data and NCAR Growing Degree Day. Remote Sensing of Environment, 161, 131-148.

Crane, M.P. and T.P. DeFelice, 2003. Enhancing the validation of remote Sensing data. AMS 12th SMOI, Long Beach, CA., 9-13 February, 001-001.

DeFelice, T.P., 2000. EDC Terrestrial-Ecosystem Assessment (TERESA) Site. Proc's USGS NMD Research Symposium, Apr. 25-27, Rolla, Missouri, 24-33.

DeFelice, T.P., and B.F. Wylie, 2001. Sky type discrimination using a ground based sunphotometer. *Atmos. Res.,* **59-60**, 313-329.

DeFelice, T.P., D. Lloyd, T.T. Baltzer, D.J. Meyer, P. Piraino, (2004). Water vapor correction of the daily 1-kilometer AVHRR global land dataset. Part I: Validation and use of the Water Vapor input field. *Int'l. J. Remote Sensing,* **24**(), 001-011.In Press.

Deschamps P.Y., Herman M., Tanre D, 1983, Modeling of the atmospheric effects and its application to the remote sensing of Ocean Color, *Applied Optics* , 22 (23): 3751-3758.

Doraiswamy, P. C. & P. W. Cook (1995) Spring wheat yield assessment using NOAA AVHRR data. Canadian Journal of Remote Sensing, 21, 43-51.

O. Dubovik, B. Holben, T.F. Eck, A. Smirnov, Y.J. Kaufman, M.D. King, D. Tanré, I. Slutsker, Variability of absorption and optical properties of key aerosol types observed in worldwide locations J. Atmos. Sci., 59 (3) (2002), pp. 590-608, 10.1175/1520-0469(2002)

Friedl, M. ., McIver, D. ., Hodges, J. C. ., Zhang, X. ., Muchoney, D., Strahler, A., Schaaf, C. (2002). Global land cover mapping from MODIS: algorithms and early results. *Remote Sensing of Environment*, *83*(1-2), 287–302. http://doi.org/10.1016/S0034-4257(02)00078-0

Friedl, M. A., Sulla-Menashe, D., Tan, B., Schneider, A., Ramankutty, N., Sibley, A., & Huang, X. (2010). MODIS Collection 5 global land cover: Algorithm refinements and characterization of new datasets. Remote Sensing of Environment, 114(1), 168–182. http://doi.org/10.1016/j.rse.2009.08.016

Gao, B.-C., and Y.J. Kaufman (1993).. Water vapor retrieval from MODIS. In Vermote and Vermuelen (1998).

Hansen, M. C., & Loveland, T. R. (2012). A review of large area monitoring of land cover change using Landsat data. Remote Sensing of Environment, 122, 66–74. http://doi.org/10.1016/j.rse.2011.08.024

Hucks, J. (1998). VIIRS Testbed sensor modeling efforts, Phase I. Raytheon Systems Company Internal Memorandum Y1629.

IPO (2000). Visible/Infrared Imager/Radiometer Suite (VIIRS) Sensor Requirements Document (SRD) for National Polar-Orbiting Operational Environmental Satellite System (NPOESS) spacecraft and sensors, Rev. 3. Prepared by Assoc. Directorate for Acquisition, NPOESS Integrated Program Office, Silver Spring, MD.

Justice, C.O., Román, M.O., Csiszar, I., Vermote, E., Wolfe, R., Hook, S.J., Friedl, M., Wang, Z., Schaaf, C., Miura, T., Tschudi, M., Riggs, G., Hall, D.K., Lyapustin, A., Devadiga, S., Davidson, C., & Masuoka, E. (2013). Land and Cryosphere Products from Suomi NPP VIIRS: Overview and Status. Journal of Geophysical Research-Atmospheres, 118, 1-13, doi:10.1002/jgrd.50771.

Johnson, D. M. (2014). "An assessment of pre- and within-season remotely sensed variables for forecasting corn and soybean yields in the United States." Remote Sensing of Environment 141(0): 116-128.

Justice, C.O., E. Vermote, J.R.G. Townshend, R. DeFries, D.P. Roy, D.K. Hall, V.V. Salomonson, J.L. Privette, G. Riggs, A. Strahler, W. Lucht, R.B. Myneni, Y. Knjazikhin, S.W.

Running, R.R., Nemani, Z. Wan, A.R. Huete, W. van Leeuwen, R.E. Wolfe, L. Giglio, J.-P. Muller, P. Lewis, and M.J. Barnsley (1998). The Moderate Resolution Imaging Spectroradiometer (MODIS): Land remote sensing for global change research, IEEE Trans. Geosci. Remote Sens., 36, 1228-1249.

Key, J. R., P. Yang, B. A. Baum, S. L. Nasiri (2000). Parameterization of shortwave ice cloud optical properties for various particle habits. Submitted to *Journal of Geophysical Research*.

Kneizys, F.X., L.W. Abreu, G.P. Anderson, J.H. Chetwynd, E.P. Shettle, A. Berk, L.S. Bernstein, D.C. Robertson, P. Acharya, L.S. Rothman, J.E.A. Selby, W.O. Gallery, and S.A. Clough (1996). *The MODTRAN 2/3 Report and LOWTRAN 7 Model*. L.W. Abreu and G.P. Anderson, eds. Prepared by Ontar Corporation, North Andover, Massachussets, for Phillips Laboratory, Geophysics Directorate, Hanscom AFB, Massachussets.

S.Y. Kotchenova, E.F. Vermote, R. Matarrese, & F.J. Klemm, Jr., Validation of a vector version of the 6S radiative transfer code for atmospheric correction of satellite data. Part I: Path radiance, *Applied Optics, Vol. 45, No. 26, p. 6762-6774., 2006*

S.Y. Kotchenova & E.F. Vermote, Validation of a vector version of the 6S radiative transfer code for atmospheric correction of satellite data. Part II: Homogeneous Lambertian and anisotropic surfaces, *Applied Optics, Vol. 46, No. 20, p. 4455-4464., 2007.*

S. Y. Kotchenova, E. F. Vermote, R. Levy, and A. Lyapustin, Radiative transfer codes for atmospheric correction and aerosol retrieval: intercomparison study, *Applied Optics, Vol. 47, No. 13, p. 2215-2226, 2008.*

Lee, T. Y., and Y. J. Kaufman (1986). Non-Lambertian effects on remote sensing of surface reflectance and vegetation index. *IEEE Transactions on Geoscience and Remote Sensing,* GE-24, 699-708.

Liang, S., others (2002). Validating MODIS land surface reflectance and albedo products: methods and preliminary results. *Remote Sensing of Environment*, **83** 001-014.

Lyapustin, A.I. (2001). Three-Dimensional Effects in the Remote Sensing of Surface Albedo. *IEEE Trans Geosci Remote Sens.,* Vol 39, 001-009.

Lyapustin, A., Wang, Y., Laszlo, I., Kahn, R., Korkin, S., Remer, L., Levy, R. & Reid, J. S. (2011). Multiangle implementation of atmospheric correction (MAIAC): 2. Aerosol algorithm. Journal of Geophysical Research: Atmospheres (1984–2012), 116(D3).

Meroni, M.; Marinho, E.; Sghaier, N.; Verstrate, M.M.; Leo, O. Remote sensing based yield estimation in a stochastic framework—Case study of durum wheat in Tunisia. Remote Sens. 2013, 5, 539–557.

Miura, T., Turner, J.P., & Huete, A.R. (2013). Spectral Compatibility of the NDVI Across VIIRS, MODIS, and AVHRR: An Analysis of Atmospheric Effects Using EO-1 Hyperion. IEEE Transactions on Geoscience and Remote Sensing, 51, 1349-1359, doi:10.1109/TGRS.2012.2224118.

Morisette, J.T., Privette, J.L., & Justice, C.O. (2002). A framework for the validation of MODIS land products. Remote Sensing of Environment, 83, 77-96, doi:10.1016/S0034-4257(02)00088-3.

Obata, K., Miura, T., Yoshioka, H., & Huete, A.R. (2013). Derivation of a MODIS-compatible enhanced vegetation index from visible infrared imaging radiometer suite spectral reflectances using vegetation isoline equations. Journal of Applied Remote Sensing, 7, 073467-073467, doi:10.1117/1.JRS.7.073467.

Pinter, P. J., R. D. Jackson, S. B. Idso & R. J. Reginato (1981) Multidate spectral reflectances as predictors of yield in water stressed wheat and barley. International Journal of Remote Sensing, 2, 43-48.

Roger, J.C., Vermote, E., Devadiga, S, and Ray J.P. (2016) Suomi-NPP VIIRS Surface Reflectance User's Guide – V1 Re-processing (NASA land SIPS), Version 1.1, VIIRS document.

Running, S. W., C. Justice, V. Salomonson, D. Hall, J. Barker, Y. Kaufman, A. Strahler, A. Huete, J.-P. Muller, V. Vanderbilt, Z. M. Wan, P. Teillet and D. Carneggie (1994). Terrestrial remote sensing science and algorithms planned for EOS/MODIS. *Int. J. Rem. Sens.*, **15(17)**, 3587-3620

Schaaf, C. B., Gao, F., Strahler, A. H., Lucht, W., Li, X., Tsang, T., … Roy, D. (2002). First operational BRDF, albedo nadir reflectance products from MODIS. Remote Sensing of Environment, 83(1-2), 135–148. http://doi.org/10.1016/S0034-4257(02)00091-3

Tanré, D., B.N. Holben, and Y.J. Kaufman (1992). Atmospheric Correction algorithm for NOAA-AVHRR Products: Theory and Application. *IEEE Transaction on Geoscience and Remote Sensing*, **30**, 231-248.

Teillet, P.M. (1991). Radiometric and atmospheric correction procedures for AVHRR preprocessing in the solar reflective channels. *Proceedings of the Fifth International Colloquium on Measurements & Signatures in Remote Sensing, Courchevel, France,* Jan. 14-18, 101-104. Canada Centre Remote Sensing (CCRS) No. ESA-319; Remote Sensing on-line Retrieval System (RESORS) ID# 1083741. {Available from Author at CCRS, 588 Booth St., Ottawa, Ontario K1A 0Y7, Canada}.

Teillet, P.M. (1992). An algorithm for the radiometric and atmospheric correction of AVHRR data in the solar reflective channels. *Remote Sensing Environment,* **41**, 185-195.

Tucker, C. J., B. N. Holben, J. H. Elgin & J. E. McMurtrey (1980) Relationships of spectral data to grain yield variation. Photogrammetric Engineering and Remote Sensing, 46, 657-666.

Vargas, M., Miura, T., & Shabanov, N. (2013). An Initial Assessment of the Suomi NPP VIIRS Vegetation Index EDR.Journal of Geophysical Research-Atmospheres, doi:10.1002/2013JD020439.

Vermote, E.F. (2003). Adjacency effect. Encyclopedia of Optical Engineering, Marcel Dekker, Inc., NY, NY, 39-48.

Vermote, E.F., and A. Vermeulen (1999). Atmospheric correction algorithm: spectral reflectances (MOD09). Version 4.0. Algorithm technical background document. *NASA EOS-1D 2015 Doc.*

Vermote, E.F., D. Tanré, J.L. Deuzé, M. Herman, and J.J. Morrisette (1994). Second Simulation of the Satellite Signal in the Solar Spectrum (6S), 6S Version 0 User's Guide, April 18. *NASA Goddard Space Flight Center,* 183 pp.

Vermote, E.F., D. Tanré, J.L. Deuzé, M. Herman, and J.J. Morrisette (1997). Second Simulation of the Satellite Signal in the Solar Spectrum, 6S: An Overview. *IEEE Transactions on Geoscience and Remote Sensing,* 35, 675-686.

Vermote, E. F., and S. Kotchenova (2008), Atmospheric correction for the monitoring of land surfaces, *Journal of Geophysical Research-Atmospheres*, *113*(D23).

Vermote, E., Justice, C. O., & Bréon, F. M. (2009). Towards a generalized approach for correction of the BRDF effect in MODIS directional reflectances. IEEE Transactions on Geoscience and Remote Sensing, 47(3), 898–908. http://doi.org/10.1109/TGRS.2008.2005977

Vermote, E., Justice, C.O., Csiszar, I.A., (2014). Early evaluation of the VIIRS calibration, cloud mask and surface reflectance Earth data records, Volume 148, 25 May 2014, Pages 134-145. doi: 10.1016/j.rse.2014.03.028

Vogelmann, J.E., and T.P. DeFelice (2003). Characterization of intra-annual reflectance properties of land cover classes in southeastern South Dakota using Landsat TM and ETM+ data. *Can. J. Remote Sens.* **29**(2), 219-229.

Wolfe, R.E., Lin, G., Nishihama, M., Tewari, K.P., Tilton, J.C., & Isaacman, A.R. (2013). Suomi NPP VIIRS prelaunch and on-orbit geometric calibration and characterization. Journal of Geophysical Research: Atmospheres,doi:10.1002/jgrd.50873

Zhan, X., Sohlberg, R. ., Townshend, J. R. ., DiMiceli, C., Carroll, M. ., Eastman, J., DeFries, R. . (2002). Detection of land cover changes using MODIS 250 m data. *Remote Sensing of Environment*, *83*(1-2), 336–350. http://doi.org/10.1016/S0034-4257(02)00081-0

END OF DOCUMENT